SCIENTIFIC REPORTS
nature research

OPEN

A Hybrid {Silk@Zirconium MOF} Material as Highly Efficient As^{III}-sponge

Yiannis Georgiou[1,2], Sofia Rapti[1], Alexandra Mavrogiorgou[1], Gerasimos Armatas[3], Manolis J. Manos[1,4], Maria Louloudi[1,4] & Yiannis Deligiannakis[2,4,5] ✉

Exposure of humans to Arsenic from groundwater drinking sources is an acute global public health problem, entailing the urgent need for highly efficient/low-cost Arsenite (As^{III}) up-taking materials. Herein we present an innovative hybrid-material, ZrMO*F*@SF_d operating like an "As^{III}-sponge" with unprecedented efficiency of 1800 mg As^{III} gr^{-1}. ZrMOF@SF_d consists of a neutral Zirconium Metal-Organic Framework [ZrMOF] covalently grafted on a natural silk-fiber (SF_d). ZrMOF itself exhibits As^{III} adsorption of 2200 mg gr^{-1}, which supersedes any -so far- known As^{III}-sorbent. Using XPS, FTIR, BET-porosimetry data, together with theoretical Surface-Complexation-Modeling (SCM), we show that the high-As^{III}-uptake is due to a sequence of two phenomena:[i] at low As^{III}-concentrations, surface-complexation of H_3AsO_3 results in As^{III}-coated voids of ZrMOF, [ii] at increased As^{III}-concentrations, the As^{III}-coated voids of ZrMOF are filled-up by H_3AsO_3 *via* a partitioning-like mechanism. In a more general context, the present research exemplifies a mind-changing concept, i.e. that a "partitioning-like" mechanism can be operating for adsorption of metalloids, such as H_3AsO_3, by metal oxide materials. So far, such a mechanism has been conceptualized only for the uptake of non-polar organics by natural organic matter or synthetic polymers.

Arsenic exposure through drinking water sourced from groundwater, is a global public health problem that is particularly devastating in certain highly populated countries[1,2]. According to a 2000 to 2010 case study, 35 to 77 million people in areas of Bangladesh or India have been chronically exposed to arsenic in their drinking water in what described as the most significant mass poisoning in history[3]. Arsenic is a naturally occurring metalloid, also released to the environment *via* anthropogenic activities. Arsenic strongly binds to proteins, so traces of this element can cause severe health problems to all life forms[4]. The predominant forms of arsenic in the aquatic environment are As^{III} (arsenite) and As^{V} (arsenate). As^{III} is more hazardous than As^{V}, as it is more mobile/bioavailable, thus more toxic[5]. This toxicity is due to its dominant H_3AsO_3 form, i.e. the predominating species in a wide range of pH < 9[6], typically encountered in natural waters. So far, traditional ion-exchange materials and sorbents, e.g. zeolites, clays, layered double hydroxides, resins have been used as arsenic adsorbends, however, with limited efficiency *vs*. As^{III} [7,8].

Given that As^{V}, which exists as anion at pH > 2, is easier to adsorb on cationic surfaces, to overcome the low efficiency of As^{III} uptake, an extra step of oxidation of As^{III} to As^{V} can be chosen before the application of various remediation technologies. Such oxidative pretreatment, however, suffers from the presence of multiple substances that interfere with As^{III} oxidation[9,10]. Therefore, it will be desirable to develop sorbents that could *directly* capture As^{III} in natural pH conditions, without the need for the oxidation to As^{V}. Several materials have been investigated for the direct removal of As^{III}, including TiO_2 nanoparticles[11], iron-based nanoparticles, e.g. zero-valent Fe nanoparticles[12–14], carbon nanotubes[15]. Such sorbents with high specific surface area and various functional groups seem promising for As^{III} remediation[16–18].

A further hurdle to overcome concerns cost-criteria, i.e. the required mass of an As^{III}-uptaking material, should be considered on a cost-efficiency basis together with the ecological impact of such sorbents is natural or

[1]Laboratory of Biomimetic Catalysis and Hybrid Materials, Department of Chemistry, University of Ioannina, GR45110, Ioannina, Greece. [2]Laboratory of Physical Chemistry of Materials and Environment, Department of Physics, University of Ioannina, GR45110, Ioannina, Greece. [3]Department of Materials Science and Technology, University of Crete, Heraklion, 71003, Greece. [4]Institute of Materials Science and Computing, University Research Center of Ioannina, GR45110, Ioannina, Greece. [5]Institute of Environment & Sustainable Development, University Research Center of Ioannina, GR45110, Ioannina, Greece. ✉e-mail: ideligia@uoi.gr

urban water bodies. So far, most of the available materials have sorption capacities of the range 60–150 mg g^{-1} [19–21], while less than five materials achieving sorption capacities > 300 mg g^{-1} [22,23]. In one report in 2014[23], the highest –so far- As^{III} uptake reported was 320 mg gr^{-1} by a hybrid consisting of Fe_2O_3 nanoparticles dispersed on a macroporous silica. Our systematic efforts during the last decade led to a series of nanomaterials with promising performances, e.g. a mesoporous spinel $CoFe_2O_4$[24] with an uptake of 252 mg As^{III} g^{-1}, magnetic carbon nanocages[22] with a sorption capacity of 264 mg As^{III} g^{-1} and MIL-100(Fe)[16] showing uptake of 120 mg As^{III} g^{-1}.

Regarding the physicochemical As^{III}-uptake mechanism, so far, in all well-understood cases, the underlying theoretical mechanism is that originally developed by Goldberg[25,26] and Manning[7,10], which entails that: [i] As^{III}-uptake by solid materials is determined by surface complexation of the As^{III} species. [ii] at pH range 5–8, i.e. typical for natural waters, the dominant species is the neutral form H_3AsO_3[27,28]. Thus –so far – the strategy by all research groups, including us[16,22,29], was to maximize the number and accessibility of surface sites based on diligent preparation protocols. In this way, it has been achieved a max As^{III}-uptake capacity 320 mg gr^{-1} by γ-Fe_2O_3 nanoparticles encapsulated in a macroporous Silica[23]. Recent data show that certain carbon based materials i.e. graphene-based[30] or more innovative graphydine[31–33] have a promising potential for adsorbing heavy metals, metalloids and other pollutants from water. In addition, some of the metal-loaded materials can have enhanced catalytic fucntionalities[34–37].

Within this frame of thinking, aiming at maximization of the surface sites, it becomes obvious that for any material, the theoretical upper limit would be determined by the site-density and the surface area:

$$N_{max}(sites/gram) = SSA(m^2/gr) \times Ns(sites/nm^2) = 10^{18} \times SSA(nm^2/gr^1) \times Ns(sites/nm^2) \quad (1)$$

Using this expression, a material whose maximum- As^{III} uptake capacity is determined by surface-adsorption has an upper theoretical limit, which under ideal conditions, would be determined by its specific surface area (SSA) and the number of surface sites (Ns). In real systems, this maximum-uptake would be further limited by the binding constant of As^{III}-on the surface-sites. On the other hand, in natural systems, Soil Organic Matter is known to be able to sequester non-polar organics *via* a partitioning-sequestration mechanism[38]. This phenomenon is based on the fundamental concept of the *partitioning* of a non-polar organic between a polar and a non-polar solvent, e.g. for example, the partitioning of phenol on [octanol: water][39,40]. Within a technological context, when partitioning is operating, a significant mass of sorbent can be transferred in the apolar matrix, thus resulting in cost-effective molecular-separation approaches[41,42]. So far, however, such a profitable concept has not been applied to attack problems such as As^{III}-remediation. Herein we introduce a mind-changing approach by developing a Zirconium Metal-Organic Framework [$[Zr_6O_4(OH)_4(NH_2BDC)_6]$ (NH_2-BDC^{2-} = 2-amino-terephthalate) [herein codenamed ZrMOF] which is able to perform a partitioning-like As^{III}-uptake thanks to the microenvironment of its pores. As we show, this approach allows an unprecedented As^{III}-uptake efficiency of > 2000 mg As^{III} per gram of ZrMOF.

Metal-organic frameworks (MOFs), which are crystalline porous materials are constituted by metal ions or metal clusters, and polytopic organic ligands, have emerged as a new class of sorbents with a promise for various remediation processes[43–45]. MOFs combine extremely high surface areas, well-defined pores, and a variety of functional groups. Furthermore, several MOFs show remarkable thermal (up to 400–500 °C) and chemical stability e.g. high resistance to acid or base[46,47]. Recently, several MOFs have been investigated as arsenic sorbents, mostly concerning investigations of forms of ionic-As^V sorption[48–50]. Only a few reports exist on the capture of As^{III} by MOFs[40,43–45]. These sorbents, however, demonstrated only moderate sorption capacities (<150 mg As^{III} g^{-1})[51].

Apart from the challenge of As^{III}-uptake efficiency, the efficient large-scale utilization of As^{III}-uptaking materials[52–54], requires their post-synthesis engineering to be usable for large-water body cleaning. The technology of grafting of the functional material on a macroscopic surface allows scale-up handling and usage. Herein we have used woven silk fibers [SF_d] as a scaffold for grafting of the ZrMOF material. The so-obtained hybrid material ZrMOF@SF_d retains the very high As^{III} sorption capacity of ZrMOF, i.e. reaching 1800 mg As^{III} per g^{-1} of material.

To understand the unprecedented high sorption efficiency of ZrMOF and ZrMOF@SF_d, we have carried out a detailed study ofthe As^{III}-sorption mechanism in conjunction with the dynamics of pore-filling and surface complexation. In a more general context, the present research exemplifies for the first time that a "partitioning-like" mechanism to be operating in for adsorption of metalloids, i.e., H_3AsO_3 by metal oxide materials, so far conceptualized only for synthetic polymers & natural organic matter (NOM)[55] used to uptake apolar organics[56,57].

Results and Discussion

Field Emission-Scanning electronic microscopy (FE-SEM) images showed that ZrMOF is composed of aggregated polyhedral-shape nanoparticles with size ~100–300 nm (Figure 1a1,a2). No obvious changes in shape and size of particles are observed for the material after the As^{III} sorption (Fig. 1b1,b2). The SEM micrograph for the silk fiber (SF_d) (Fig. 1c), shows the surface morphology of well-defined fibers of natural-silk. After covalent grafting of ZrMOF on the SF_d fibers, we obtain well-dispersed ZrMOF particles on the silk-fibers (Fig. 1d). Adsorption of As^{III} onto ZrMOF@SF_d does not alter the particle morphology (Fig. 1e). Thermogravimetric (TGA) analysis, Fig. S1 in Supporting Information, shows that the ZrMOF@SF_d hybrid contains 5.7% w:w of ZrMOF.

For the engineering of the ZrMOF grafting on the silk fiber, we have used natural silk tissue, which we have degummed according to established procedures (see Supporting Information, photos in Scheme S1)[58]. The degumming method of Gulrajani[58], resulted in high-quality silk-fiber, as evidenced by the SEM micrography, see Fig. 1(c), as well as the XRD pattern, Fig. 2A, which reveals retention of the fibers' order and physical integrity in the structure of the degummed silk (SF_d). After grafting of the ZrMOF@SF_d, the SEM data (Fig. 1d) shows a good dispersion of the ZrMOF particles on the silk fibers. XRD data for the ZrMOF@SF_d hybrid, Fig. 2a(red) show the characteristic reflection at 7.3° and 8.5° originating from the ZrMOF particles grafted on the silk. Notice

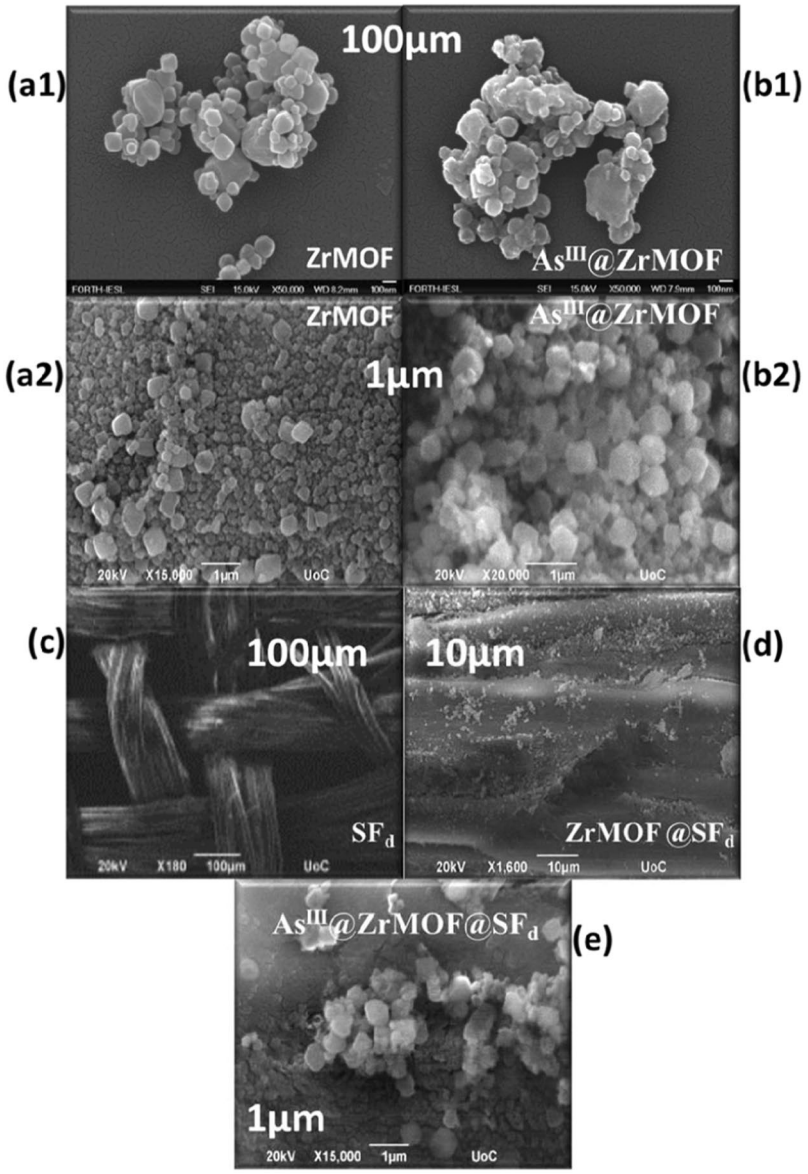

Figure 1. FE-SEM images for ZrMOF (**a1**,**a2**), As^{III}-loaded ZrMOF (**b1**,**b2**), natural-silk SF_d (**c**),ZrMOF@SF_d (**d**), As^{III}-loaded ZrMOF@SF_d (**e**).

that, upon grafting, the crystallinity of the SF_d is distorted, i.e. see the loss of the sharp peaks at 15°–17° in Fig. 2a. This result is due to molecular covalent grafting of the ZrMOF-silane on SF_d (see also Scheme S2 in Supporting Information)

TGA analysis, Fig. 2c, revealed a significant weight loss (~17.2%) in the temperature range 25 to 102 °C attributed to the release of solvent molecules, mostly MeOH. Then, there is a continuous weight loss (~7.9%) (with no discrete steps) till 302 °C, followed by an abrupt weight loss (38.8%) ending at 540 °C. Finally, there is a small weight loss (~2%) from 615 to 715 °C (Fig. 2c). The TGA residue is solid ZrO_2, as confirmed by XRD data. For 100 g of ZrMOF 33.7 g of ZrO_2 was obtained after calcination, which corresponds to ~24.9% Zr w:w. Based on this % Zr content found from TGA, the suggested formula for ZrMOF is $[Zr_6O_4(OH)_4(NH_2\text{-}BDC)_6]\cdot 12MeOH\cdot 3H_2O$ (calculated % Zr = 24.96).

The pristine silk fabric (SF) and degummed silk fibroin fibers (SF_d) were characterized by FT-IR and thermogravimetric analysis (TG-DTA). The typical IR-peaks of SF are ≈1620–1700, 1511–1539, and 1226–1235 cm^{-1}, characteristic for amide I (C=O stretching), amide II (N–H deformation, and C–N stretching) and amide III (C–N stretching and N–H deformation). FT-IR (cm^{-1}, selected peaks) SF: 3533: ν(OH); 3072, 2980, 2936, 2880: ν(C-H); 1697: amide I (β-sheet); 1595: amide II (β-sheet); 1256: amide III (β-sheet), 1166: ν(C-OH). SF_d 3477: ν(OH); 3075, 2980, 2936, 2880: ν(C-H); 1708, amide I (β-sheet); 1595: amide II (β-sheet); 1271: amide III (β-sheet), 1001: ν(C-OH) (see Fig. S2). Both TG-DTA curves (see Supporting Information Fig. S1) for the SF and the SF_d show similar thermal-response behavior. At T < 110 °C the weight loss is attributed to the evaporation of water. The change from 170 °C to 275 °C can be assigned to the loss of other low-temperature volatile species, and

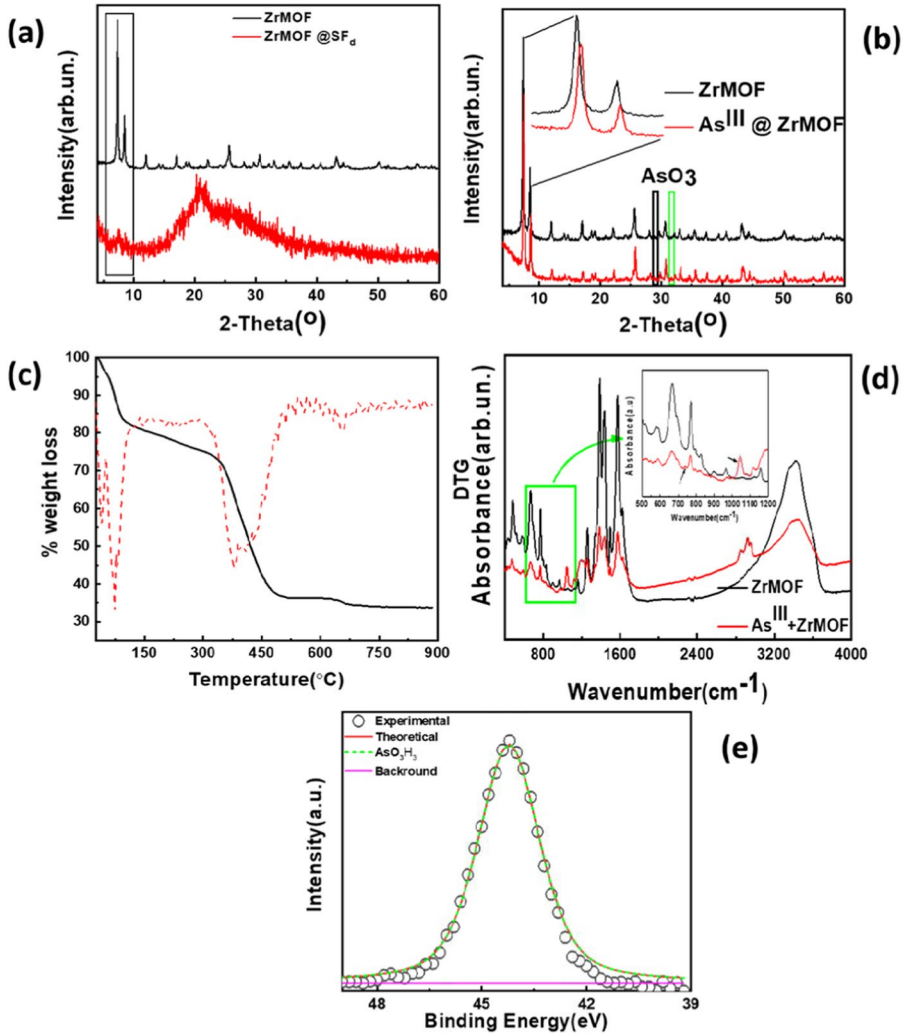

Figure 2. (**a**) PXRD data for ZrMOF and ZrMOF @ SF_d, (**b**) PXRD data for ZrMOF, and As^{III}@ ZrMOF. (**c**) TGA (solid line) and first derivative (DTG) (dashed line) plots for ZrMOF,(**d**) FT-IR spectra for pristine (—), and As^{III}-loaded ZrMOF material (—), (**e**) XPS As3d analysis for ZrMOF after As^{III} loading.

the change from 275 °C to 400 °C is associated with the breakdown of side-chain groups of amino acid residues as well as the cleavage of peptide bonds of silk fiber, and at T > 400 °C it is attributed to fibroins' degradation[59]. The TG% curves of SF and SF_d exhibit a total weight loss of 98.4% and 98.9% respectively, in the range 20–700 °C with a broad exothermic peak at 400–600 °C assigned to the fibroins' degradation. The DTA curve of SF_d also shows an intense peak at 577 °C, originating from the amorphous sericin extraction[59] and the degummed β-sheet fibroin degradation[59].

The final ZrMOF@SF_d hybrid was characterized by FT-IR and thermogravimetric analysis (TG-DTA) (see Fig. S1 in Supporting Information). The typical IR-peaks of SF are ≈1620, 1511, and 1226 cm^{-1}, characteristic for amide I (C=O stretching), amide II (N–H deformation, and C–N stretching), and amide III (C–N stretching and N–H deformation). FT-IR (cm^{-1}, selected peaks) ZrMOF@SF_d: ν(OH); ν(C-H); ν(C=C); ν(C-OH); ν(C-O) (see Fig. S1 in Supporting Information). The TG-DTA curves for ZrMOF@SF_d show a thermal-response profile similar to that of the SF_d fibers. The TG% curve of ZrMOF@SF_d exhibits a total weight loss of 97.3% in the range of 20–700 °C with a broad exothermic peak at 400–600 °C assigned to the fibroins' degradation. The DTA curve of ZrMOF@SF_d presents a shifting of the degradation temperature around T = 360 °C (compared to the SF_d DTA curve at T = 320 °C), which is attributed to the combustion of the organic part of ZrMOF@SF_d (estimated w:w ≈ 5.7%).

The FT-IR spectra for ZrMOF and As^{III}-loaded ZrMOF (Fig. 2d) are very similar, indicating the retention of the structure of the ZrMOF after As^{III} sorption. Noteworthy, in the IR spectrum of As^{III} @ ZrMOF, there is a band around 740 cm^{-1} and 1040 cm^{-1}, which is attributed to As^{III}-O stretch from H_3AsO_3[25,48,60,61].

X-ray photoelectron (XPS) analysis was used to determine the As^{III}-valence state and the eventual interaction between arsenic and the adsorbent. The high-resolution As3d XPS spectrum, shown in Fig. 2e, clearly indicates that As^{III} is the only oxidation form adsorbed onto ZrMOF sorbent. The characteristic peak at 44.2 eV corresponds to As^{III} in agreement with Sudhakar *et al.*[62], while no peak corresponding to As^{V} is detected in As-loaded

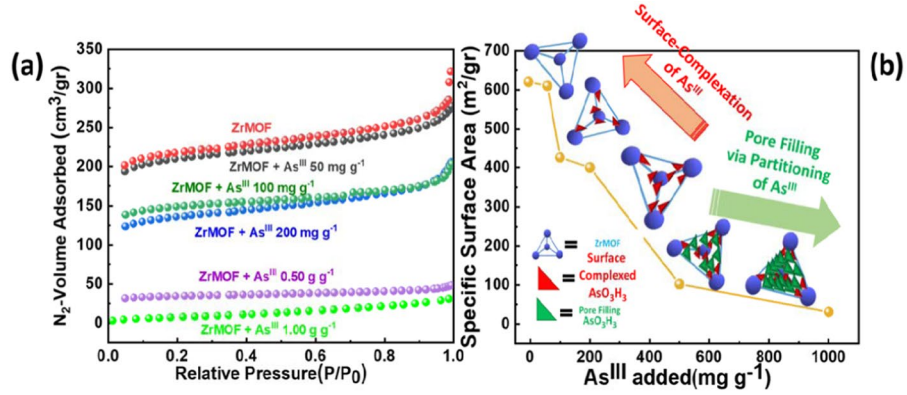

Figure 3. (**a**) Nitrogen sorption isotherms at 77 K for ZrMOF and As^{III}@ZrMOF for different As^{III} loadings (**b**) BET surface area *vs*. As^{III} loading.

ZrMOF. This result shows that after adsorption of the As^{III} on the ZrMOF, there is no oxidation event of As^{III} , thusall the bound As atoms on ZrMOF are in the As^{III} oxidation form. This information is in agreement with our FT-IR data, which detects the As^{III}-O stretch, Fig. 2d, originating from H_3AsO_3. Also, the prevalence of the H_3AsO_3 form is corroborated hereafter by the adsorption-isotherms' analysis, which shows that the adsorbed species is exclusively the neutral form of $As^{III,}$ i.e., $H_3As^{III}O_3$.

ZrMOF is a highly porous material with a 12-connected net based on $[Zr_6O_4(OH)_4]$ hexanuclear units interconnected via NH_2-BDC^{2-} ligands. We should note that pZrMOF is charged due to the protonation of amine groups (as the ZrMOF is prepared in acidified water). Prior to the As^{III} sorption investigations, the ZrMOF was treated with MeOH/Et_3N to deprotonate the amine groups, thus resulting in a neutral framework.

A severe decrease of the Specific Surface Area of the ZrMOF is observed upon As^{III} adsorption, see Fig. 3a,b. The non-linear [SSA *vs*. As^{III}] trend in Fig. 3b, for ZrMOF can be analysed into two different domains: [i] at low As^{III}-loading the SSA is decreased moderately, [ii] at high-As^{III} loading there is an abrupt lowering of the SSA. This change in SSA is not due to alteration of the crystal structure of ZrMOF, as verified by PXRD, Fig. 2b. Thus, the severe decrease of SSA upon As-uptake provides important insight into the As^{III}-uptake mechanism by ZrMOF as follows: the SSA of 610 $m^2\ gr^{-1}$ for ZrMOF is equivalent to 6.1×10^{20} nm^2 per gram of ZrMOF. The molecular volume of H_3AsO_3 in H_2O has been estimated by Canaval *et al.*[63] to be $75 \pm 10 Å^3$. Accordingly, each nm^2 surface element of ZrMOF can accommodate not more than 2 H_3AsO_3 molecules, which gives an N-maximum of surface-adsorbed H_3AsO_3 molecules $N_{max} = 2$ [H_3AsO_3 per nm^2] × [6.1×10^{20} nm^2 per gram of ZrMOF] ~ 1.5mmoles of H_3AsO_3 per gram of ZrMOF. When we compare this *vs*. the maximum As^{III}-uptake capacity i.e. ~30 mmoles H_3AsO_3 per gram, we conclude that the experimental As-uptake is 20 times higher than the maximum As^{III}-uptake capacity of 1.5 mmoles of H_3AsO_3 per gram, that would correspond to a mere surface coverage. Instead, the SSA drop *vs*. As-uptake data in Fig. 3b indicates a pore-filling mechanism, not a simple surface complexation. At the same time, the crystallinity of the ZrMOF material is retained after As^{III}-uptake, see XRD in Fig. 2b. This result makes the ZrMOF behaving like an "As^{III}-sponge" being capable of adsorbing unprecedented high-amounts, i.e., 2.2 grams of toxic As^{III} per gram of ZrMOF.

As^{III}-adsorption kinetics. Kinetic data of As^{III} adsorption by ZrMOF, Fig. 4a, show fast kinetics with a non-linear time-profile. The kinetic data can be fitted by the Weber and Morris model, described by Eq. 2[64].

$$q(t) = K_{in}t^{0.5} + C \tag{2}$$

The Weber and Morris model[64] is based on the key-assumption that diffusivity and mass- transfer phenomena are determining the adsorption process. In Eq. 2, the fittable parameters are the kinetic constant rate K_{in} ($g\ g^{-1}\ h^{1/2}$), and C ($g\ g^{-1}$) which is a constant depending on the type of the boundary layer[64]. Accordingly, the data in Fig. 4a can be fitted by considering two different sets of K_{in} and C, listed in Table S1 of the Supporting Information. At early adsorption times, (red circles in Fig. 4a), a fast kinetic constant $K_{in} = 6\,g\,g^{-1}\,h^{1/2}$ is obtained, with $C = 0.11\,g\,g^{-1}$ while at prolonged adsorption times, the kinetic constant is much lower $K_{in} = 1.9\,g\,g^{-1}\,h^{1/2}$, with $C = 1.1\,g\,g^{-1}$. This analysis reveals a two kinetic-phase phenomenon for As^{III} uptake by ZrMOF. Taking into account the analysis of SSA data, we consider that the initial fast phase, corresponding to low-As uptake, is responsible for low decrease of SSA. At prolonged interaction times, where the adsorbed As^{III} is high, a slower kinetic phase is operating, which corresponds to the sharp drop of SSA, i.e. the pores of ZrMOF are filled up with H_3AsO_3.

The same kinetic two-phase profile is observed for the ZrMOF@ SF_d hybrid, Fig. 4b, indicating that the grafted ZrMOF particles operate similarly, i.e. surface adsorption of As^{III} at low concentrations (red symbols in Fig. 4b) followed by pore filling at high As^{III}-concentrations (green symbols in Fig. 4b). The silk fiber plays a minor role in As-uptake i.e. see adsorption isotherm in Fig. 5.

As^{III}-adsorption isotherms. A non-linear isotherm characterizes the uptake of As^{III} by ZrMOF, see Fig. 5(●, ●), which can be analyzed in the two regions depending on the initial concentration of As^{III}. [i] At low

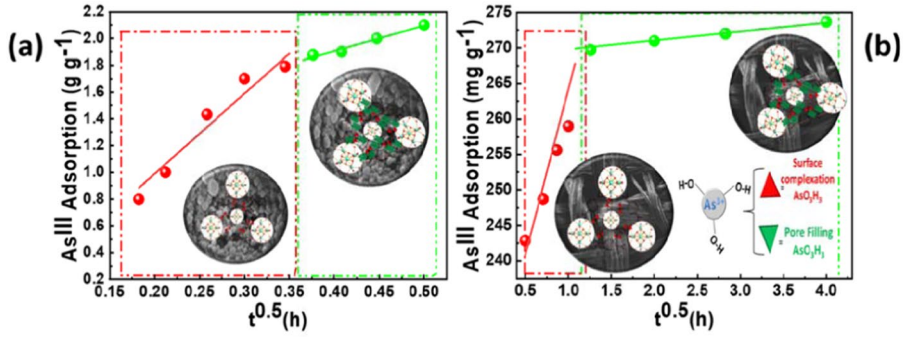

Figure 4. As^{III} adsorption kinetics for (**a**) ZrMOF and (**b**) ZrMOF@SF_d at pH 7. Symbols (,) are experimental data. Lines are theoretical curves calculated using Eq. 2, with the parameters listed in Table S1. In (**a**) the added As^{III} concentration was 50 mg L^{-1}. In (**b**) the added As^{III} concentration was 15 mg L^{-1}.

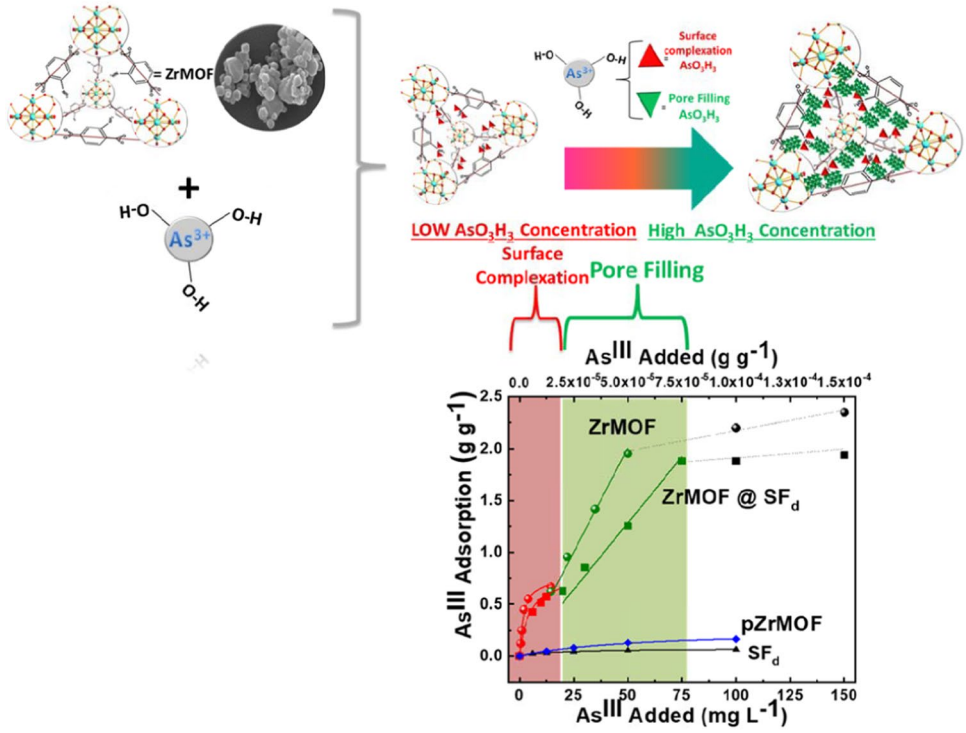

Figure 5. As^{III} adsorption isotherms for ZrMOF (, ,), ZrMOF@SF_d (, ,),pZrMOF( ), and SF_d ( ) at pH 7.

As^{III}-concentrations (<25 mg As^{III} Lt^{-1}), the isotherm shows a Langmuir-like trend, see solid-red symbols in Fig. 5( ). [ii] At increased initial As^{III} concentrations, the isotherm data show a linear As-uptake isotherm, Fig. 5( ). This trend continues up to 75–80 mg of added As^{III} Lt^{-1}. At even higher initial As^{III}, the isotherm flattens, indicating a saturation of the As^{III}-uptake by ZrMOF. Based on the data of Fig. 5, the maximum adsorbed As^{III}per gram of ZrMOF material corresponds to a maximum of 2200 mg As^{III} gr^{-1} of ZrMOF. The ZrMOF@SF_d material exhibited a similar two-isotherms profile, see Fig. 5(,) When normalized [per mass of grafted ZrMOF], the As^{III} -uptake data in Fig. 5(,) show that the performance of the ZrMOF@SF_d material is within ~10% comparable to ZrMOF. Thus, grafting of ZrMOF retains its As^{III} -uptaking capacity. For reference, pZrMOF and the SF_d alone Fig. 5( ), ( ) show a very low As^{III} -uptake, i.e. 0.260 g g^{-1}, and 0.068 g g^{-1} respectevelly. The significant inhibitory effect of the cation sites in cationic pZrMOF, to As^{III} uptake i.e. *vs* the neutral ZrMOF, reveal that the surficial NH_2 sites play key role in the uptake mechanism. This is further analyzed in the following in the theoretical surface Complexation Modeling hereafter.

Theoretical modeling of the data in Fig. 5 can be done using two isotherm-adsorption models. [a] *At low added-As^{III} concentrations*, a Langmuir equation (Eq. 3) describes adequately the process, see fit (red line in Fig. 5)

Materials	Langmuir			Freundlich			
	q_m(g g^{-1})	K_{ads}	R^2	q^{Part}(g g−1)	n	K_{Part}	R^2
ZrMOF	0.83	0.18	0.990	2.20	1	0.04	0.989
ZrMOF@ SF$_d$	0.14	0.063	0.988	1.80	1	0.0045	0.974
pZrMOF	0.017	0.260	0.994				
SF$_d$	0.071	0.068	0.984				

Table 1. Parameters for Langmuir isotherms and Freundlich isotherms, used to fit the experimental data for As^{III} binding onto pZrMOF, ZrMOF, $SF_{d,}$ and ZrMOF@ *SF$_d$* at pH 7.

where q_m (mg g^{-1}) is maximum As^{III} adsorption, q^L_{ADS} (mg g^{-1}) is the surface concentration of adsorbed As^{III} species in materials. C_e (mg L^{-1}) is the initial As-concentration. $K_{Langmuir}$ is the Langmuir stability constant representing the strength of As^{III}-binding of the ZrMOF surface[65].

$$q^{L}_{\mathrm{ADS}} = \frac{q_m{}^{*}K_{\mathrm{Langmuir}}{}^{*}C_e}{1 + K_{\mathrm{Langmuir}}{}^{*}C_e} \tag{3}$$

[b] *At increased added-As^{III} concentrations*, we consider a linear Freundlich-type isotherm (Eq. 4)

$$q^{\mathrm{Part}}_{\mathrm{Ads}} = K_{\mathrm{part}} C_e^{\frac{1}{n}} \tag{4}$$

where q^{Part} gives the bound As^{III} -moieties in the ZrMOF, in mg g^{-1}. The index n reflects a constant related to the intensity of sorption or the degree of the dependence of sorption on concentration. The efficiency of uptake is classified according to the value of K_{part}. The linear Freundlich-type adsorption isotherms can be used to describe pore filling/partitioning processes[66] in hydrophobic/hydrophilic interfaces.

Using the two isotherms Eqs. 3 and 4, the data in Fig. 5 can be fitted (see solid lines in Fig. 5) with the parameters listed in Table 1. More specifically, at low As^{III}-concentrations, the uptake capacity -due to surface complexion- can achieve a maximum of $q_m = 0.83\,g\,g^{-1}$of As^{III} at pH = 7. At high As^{III}-concentration, where pore filling is operating, Fig. 5 (green line) a maximum As-uptake is attained of $q_e = 2.2\,g\,g^{-1}$of As^{III} at pH = 7.

Further analysis of the surface adsorption for the As^{III} species can be done by modeling of the pH-dependent As-uptake on the ZrMOF. This analysis, detailed in our previous works[16,24,67], is described in Supporting Information, Fig. S4. According to Fig. S4, the pH-dependent profile for low As^{III}-concentrations shows that As^{III} binds in its neutral form H_3AsO_3 at the neutral amino-sites of neutral ZrMOF. This result is in agreement with Georgiou *et al.*[16], Gupta *et al.*[27], Su and Puls[28]. The surface amines $\equiv NH_2$ act a specific binding sites for As^{III}-uptake, see reaction (15), and (17) $\equiv NH_2 + H_3AsO_3 \leftrightarrow \equiv NH_2\text{-}[H_3AsO_3]$ in Table S2. We underline that in the cationic pZrMOF, the protonated $\equiv NH_3{}^+$ sites, reaction (12) in Table S2, do not favor adsorption of As^{III} and this is the origin of the inferior performance of pZrMOF *vs*. ZrMOF. This is structurally described in Fig. S4d.

Since, in natural waters, several ions may coexist with arsenic, these can potentially compete with As-uptake[68]. In this context, the impact of competing ions such as $PO_4{}^{3-}$, $CO^{2-}{}_{3,}$ $NO_3{}^-$, $^{SO2-}{}_4$, Cl^- and $HCO_3{}^-$ on As^{III} adsorption was studied, see Fig. S5 in the Supporting Information. The data in Fig. S5, indicate that ZrMOF and ZrMOF@ SF_d effectively remove As^{III} even in the presence of $CO_{3,}$ $NO_3{}^-$, , $SO_4{}^{2-}$, Cl^- and $HCO_3{}^-$. The stronger inhibitory effect is exerted by $PO_4{}^{3-}$ ions which may inhibit As^{III} adsorption by 40% and 60% for ZrMOF and ZrMOF@$SF_{d,}$ respectively. The results are well agreement with Sudhakar[62] *et al.* and Jain and Loeppert[69], which point out that the natural water ions do not affect the As^{III} adsorption except for $PO_4{}^3$ which destabilizes the MOF structure.

Finally, we have evaluated the possibility of reusing the ZrMOF and ZrMOF@SF_d materials after regeneration. Thus, we have applied the regeneration protocol[24,70], which involved high ionic-strength treatment. More particularly, the protocol involves incubation for 24 hours under stirring at a pure aqueous solution containing 1 M of KNO_3. Our data show that the As^{III} adsorbed on either ZrMOF or ZrMOF@SF_d cannot be removed by this treatment, indicating the high stability of the bound As^{III}, i.e. attributed to its irreversible penetration into the pores of the ZrMOF.

Comparison of As^{III}-uptake with similar metal-organic framework materials. Figure 6 summarizes a comparison of As^{III} sorption by the present materials *vs*. other pertinent MOF-based materials reported in the literature. According to Fig. 6, ZrMOF supersedes by far any known material.

This result is attributed to the fundamentally different mode of action of the neutral ZrMOF, i.e. the partitioning-like mechanism resulting in pore-filling allows exploitation of the full pore volume as a "sponge" for the uptake of the As^{III} species form solution.

Conclusions

Using XPS, FTIR, BET-porosimetry data, with theoretical Surface-Complexation-Modeling (SCM), we report a two-step phenomen non which boosts high-As^{III}-uptake. First, at low As^{III}-concentrations, surface-complexation of H_3AsO_3 results in As^{III}-coated voids of neutral ZrMOF, and subsequently, at high As^{III}-concentrations, the As^{III}-coated voids of neutral ZrMOF are filled-up by H_3AsO_3 *via* a partitioning-like mechanism. Also, we present an innovative hybrid-material, ZrMO*F@SF$_d$* operating like an "As^{III}-sponge" with unprecedented efficiency of 1800 mg As^{III} gr^{-1}. ZrMOF@*SF$_d$* consists of a Zirconium Metal-Organic Framework [ZrMOF] covalently grafted

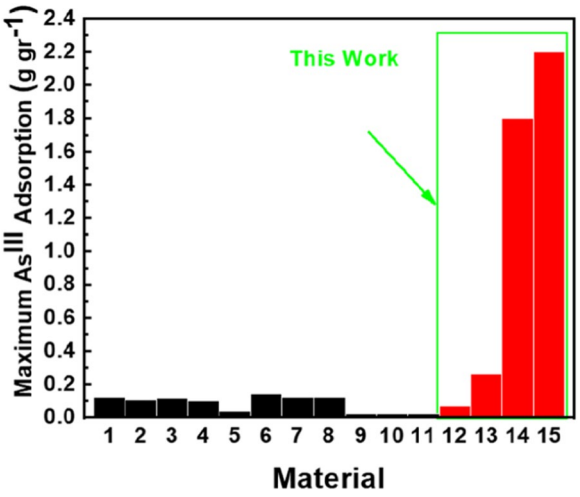

Figure 6. Maximum As^{III} adsorption capacity (g g^{-1}) at waters' near-neutral pH of some adsorbents reported in the literature compared with the present materials: 1) ZIF-8(cubic)[77], 2) ZIF-8(leaf)[77], 3) ZIF-8 (dodecahedral)[77], 4) Fe_3O_4@ZIF-8[78],5) HCl-UiO-66$(SH)_2$[79], 6) $CoFe_2O_4$@MIL-100(Fe)[48], 7) Fe_3O_4@MIL-101[80], 8) MIL-100(Fe)[16], 9) M600[16], 10) M800[16], 11) M900[16], 12) ZrMOF(this work), 13) cationic pZrMOF (this work), 14) SF_d (this work), 15)neutral ZrMOF@SF_d (this work).

on *SF_d*. ZrMOF itself exhibits As^{III} adsorption of 2200 mg gr^{-1}, which supersedes any -so far- known As^{III}-sorbent. The reference materials i.e. cationic-pZrMOF and SF_d play secondary role in As^{III}-adsorption with adsorption capacity 260 mg As^{III} gr^{-1} and 68 mg As^{III} gr^{-1} respectively. Finally, the present research exemplifies for the first time a novel concept of a "partitioning-like" mechanism, operating for adsorption of H_3AsO_3 , by neutral metal oxide materials. So far, such a mechanism has been conceptualized only for the uptake of non-polar organics by natural organic matter or synthetic polymers.

Methods

Materials. Sodium meta-arsenite $NaAsO_2$ was obtained from Sigma-Aldrich, while HCl, NaOH, KNO_3, and Cu $(NO_3)\cdot 3H_2O$ obtained from Merck. 2-(N-Morpholino)ethanesulfonic acid hydrate, 4-Morpholineethanesulfonic acid (call MES hydrate) & 4-(2-Hydroxyethyl)piperazine-1-ethanesulfonic acid, N-(2-Hydroxyethyl)piperazine-N-(2-ethanesulfonic acid)(call HEPES), used for pH buffering, were obtained from Sigma-Aldrich. Milli-Q Academic system, Millipore produced ultrapure water.

The Silk Fabric (SF) provided by Tsiakiris Georgios Silk Company, Alexandroupoli, Greece. Sodium carbonate (Na_2CO_3) purchased from Riedel de Haën. The coupling agent 3-(chloropropyl)trimethoxysilane was provided by Fluka. Methanol and ethanol purchased from Merck and diethyl ether from Sigma Aldrich.

All reagents were of analytical reagent grade purity, and all solutions prepared using deionized water obtained with a Milli-Q system with a conductivity of 18.2 μS cm^{-1}.

ZrMOF preparation. The protonated (cationic) $[Zr_6O_4(OH)_4(NH_3^+\text{-}BDC)_6]Cl_6\cdot 35H_2O$ (herein codenamed as pZrMOF) was synthesized as described previously[71]. To prepare the neutral material, pZrMOF (100 mg, 0.038 mmol) was treated with Et_3N (72.6 mg, 0.7 mmol) in MeOH (4 mL) for 1 h. The resulting solid $[Zr_6O_4(OH)_4(NH_2\text{-}BDC)_6]\cdot x$MeOH$\cdot y H_2O$ (herein codenamed as ZrMOF) was then isolated by filtration, washed with MeOH and dried in the air. Yield: 89%.

Degumming process of Silk Fabric (SF_d). The SF cut in pieces of 3.3 × 0.9 cm (≈15 mg), which were immersed into a 200 ml round-bottom flask and were degummed in a 0.05 wt.% Na_2CO_3/H_2O solution at 90 °C for 30 min and then rinsed thoroughly with double distilled water to extract the sericin protein and other impurities. This process repeated three times to obtain pure silk fibroin fibers (SF_d). The degummed silk fibroin fibers (SF_d) dried at 40 °C under atmospheric pressure.

Covalent grafting of ZrMOF on SF_d (ZrMOF@SF_d). A solution of ZrMOF (0.066 mmol) in 10 ml of methanol prepared for sonicating to achieve a good suspension in the dispersion media. After 0.022 mmol of 3-(chloropropyl) trimethoxysilane sonicated added in the solution, and finally, the reaction mixture refluxed at 60 °C for 48 h. The molar ratio of ZrMOF/silane was 3:1. To this, 30 mg of degummed SF_d fibers and 5 ml of ethanol were added and refluxed at 60 °C for 24 h. The degummed SF_d fibers (30 mg) immersed into 10 ml of ethanol for 24 h, before modification with ZrMOF/silane. After cooling at room temperature, the resulting material, ZrMOF@SF_d was washed several times with methanol, ethanol, and diethyl ether and dried under vacuum at 40 °C for 24 h.

Physical characterization of materials. EDS analysis for ZrMOF showed no Cl confirming the complete deprotonation of ammonium groups. The powder X-ray diffraction (PXRD) measured at room temperature on an STOE-STADIMP powder diffractometer. PXRD equipped with an asymmetrically curved Germanium monochromator (CuKα1 radiation, $\lambda = 1.54056$ Å) and a one-dimensional silicon strip detector (MYTHEN2 1 K from DECTRIS). The line focused Cu X-ray tube operated at 40 kV and 40 mA. Powder of each sample was packed in a 1 mm diameter polyimide capillary (polymer substrate with neither Bragg reflections nor broad peaks above 10 °) and measured in Debye-Scherrer geometry on a spinning stage (~200 rpm). Intensity data from 3 to 125 degrees 2Θ collected for 17 h with a step of 0.005 degrees. The instrument calibrated against a NIST Silicon standard (640d) before the measurement.FT-IR spectra were recorded on KBr pellets in the 4000-400 cm^{-1} range using a Perkin-Elmer Spectrum GX spectrometer. Thermogravimetric analyses (TGA) were performed on a NETZSCH STA 449 C system. Sample analysis was conducted from 25 to 900 °C in an air atmosphere (50 mL min^{-1} flow rate) with a heating rate of 10 °C min^{-1}. Scanning electron microscope (SEM) performed by a JEOL JSM-6390LV equipped with an Oxford INCA PentaFET-x3 energy-dispersive X-ray spectroscopy (EDS) detector. Data acquisition performed with an accelerating voltage of 20 kV and 120 s accumulation time. Then the images were taken with a field emission JEOL JSM 7000 F electron microscope operating at 15 kV accelerated voltage. The samples were sputter-coated with 5–10 nm also reduce charging by used Au film.

X-Ray Photoelectron Spectroscopy (XPS) measurements were using a SPECS GmbH. Instrument equipped with a monochromatic MgKα source ($h\nu = 1253.6$ eV) and a Phoibos-100 hemispherical analyzer. The spectra were recorded under ultra-high vacuum s with a base pressure of 2–5 × 10^{-10} mbar. Prior to measurement, the samples were placed on silicon substrates under high vacuum, before being placed in the main chamber for XPS measurement. The take-off angle was 45°. The recorded spectra were the average of three scans, with energy step 0.1–0.2 eV and a dwell time of 1 s. The As3d binding energy is calibrated based on the C1s core level at 284.5 eV. The spectral analysis included [i] a Shirley background subtraction, and [ii] peak deconvolution employing mixed Gaussian–Lorentzian functions in a least-squares curve-fitting program (WinSpec, Laboratoire Interdisciplinaire de Spectroscopie Electronique, University of Namur, Belgium)[72,73].

N_2 adsorption isotherms were measured at 77 K using a Quantachrome NOVAtouch LX^2. Before analysis, all samples were degassed at 80 °C under vacuum (<10^{-5}Torr) for 16 h. The specific surface areas were calculated by the Brumauer-Emmett-Teller (BET) method using the N_2-adsorption data points, in the relative-pressure range P/P_o of 0.05–0.35.

As^{III} analytical determination. The concentration of As^{III} in the aqueous solution determined by square wave Cathodic Stripping Voltammetry (SW-CSV) using a Trace Master5-MD150 polarograph by Radiometer Analytica. SW-CSV is well suited for the analytical determination of As^{III} [22,74] with a low detection limit (0.5 μg L^{-1}). The measuring borosilicate glass cells obtained from Radiometer Analytica. The working electrode was a hanging mercury drop electrode (HMDE) with drop diameter of 0.4 mm generated by a 70 μm capillary. An Ag/AgCl electrode with a double liquid junction used as the reference electrode with a Pt measuring electrode. Importantly, samples were not purged with N_2 gas to avoid the loss of As^{III}. During the stripping step, the solution stirred at 525 rpm. All measurements we performed using aliquots of 8.3 mL shifting at pH < 0.5 by 1.5 mL from 6.66 M of HCl and final 2 M concentration in the electrochemical cell, then 8 ppm of Cu^{2+} were added. In the following, As^{III} was determined by SW-CSV with accumulation potential E = −400 mV and accumulation time in the 60 s. As^{III} quantified by its signal at $E_{1/2} = -670$ mV[16,19,22].

As^{III} adsorption experiments. *For* the kinetic measurements, As^{III} uptake from aqueous solutions studied in batch experiments. The kinetics of As^{III} adsorption using ZrMOF studied as follows: 4 10^{-4} g L^{-1} of *ZrMOF* were dispersed in 50 mL buffered aqueous solution in polypropylene tubes at pH 7, in the presence of 50 mg L^{-1} As^{III}. For samples, ZrMOF @ SF_d 3.4 mg was dispersed in 25 mL buffered aqueous solution in polypropylene tubes at pH 7, in the presence of 15 mg L^{-1} As^{III}. The time-evolution of As^{III} concentration was monitored at contact times ranging between 0–240 min and 0–960 min, respectively. At the end of each contract period, all sample centrifugation and the supernatant solution analyzed for As^{III}. To determine the adsorption rates of As^{III}, the amount of As^{III} adsorbed at time t, q (mg As^{III} g^{-1}), calculated from the mass-balance between the initial concentration and the concentration at time t onto the solid adsorbents[16,29].

Adsorption isotherms for pZrMOF and ZrMOF were recorded at pH 7 in the presence of 0–100 mg L^{-1} $NaAsO_2$ interacting with 0.1 g L^{-1} pZrMOF and 0 to 150 mg L^{-1} $NaAsO_2$, interacting with 4 10^{-4} g L^{-1} of ZrMOF suspended in 50 mL buffer solution in polypropylene tubes. On the other hand, for *SFd and* ZrMOF @ SF_d, 0 to 100 mg L^{-1} and 0 to 150 mg L^{-1} $NaAsO_2$ and 0.2 g L^{-1},0.14 g L^{-1} respectively were suspended in 25 mL buffer solution in polypropylene tubes.

pH-dependent (pH-edge) experiments allow a detailed probing of the interfacial adsorption *mechanisms*[16,29], while adsorption isotherms report the maximum uptake capacity. In this work, pH-edge adsorption experiments carried out for an initial concentration of 5, 5, and 15 mg L^{-1}($NaAsO_2$) and also 0.1 g L^{-1},0.4 10^{-4} g L^{-1}, 0.14 g L^{-1} of pZrMOF, *ZrMOF and ZrMOF @ SF_d* respectively, suspended in 50 mL buffer solution whose pH adjusted in the range 4 to 8, in polypropylene tubes.

After metal addition, the suspension was allowed to equilibrate for 15 min ZrMOF, *and pZrMOF* at RT, while agitated using a magnetic stirrer. After completion of equilibration, the suspensions centrifuged at 6000 rpm for 10 min, and the supernatant solutions were analyzed for As^{III} as described above. For *SF_d* and ZrMOF @ *SF_d* after metal addition, the suspension was allowed to equilibrate overnight at RT while using a magnetic stirrer. After completion of equilibration, the *SF_d* or ZrMOF @ *SF_d* suspension collects by metal tweezer.

Reuse experiments were also conducted for ZrMOF, which had adsorbed As^{III} at pH 7. To reuse the samples, we had to desorb the adsorbed As. Thus, following the method used in ref. [30,75], after As^{III} adsorption, the material was immersed in an aqueous solution of 1 M KNO_3 for 24 h, and the supernatant was analyzed for As^{III}

release[24,70,76]. Similarly, the ZrMOF @ SF_d once loaded with As^{III} were washed at high ionic strength 1 M KNO_3 and the supernatant was analyzed for As^{III} release.

Control experiments (without ZrMOF, pZrMOF, SF_d, and ZrMOF @ SF_d) showed no loss of initial As^{III}. The initial pH values of buffer solutions were adjusted to the requested using small volumes of 1 M HCl or 1 M NaOH. It should mention that HCl is inert towards As^{III} in voltammetric measurements, the pH drift of each suspension, i.e. measured at the beginning and the end of incubation, was <0.2 pH units.

Received: 19 March 2020; Accepted: 17 April 2020;
Published online: 09 June 2020

References

1. Smith, A. H., Lingas, E. O. & Rahman, M. Contamination of drinking-water by arsenic in Bangladesh: a public health emergency. *Bull. World Health Organ.* **78**, 1093–1103 (2000).
2. Ravenscroft, P., Brammer, H. & Richards, K. *Arsenic pollution: a global synthesis*. vol. 28 (John Wiley & Sons (2009).
3. Flanagan, S. V., Johnston, R. B. & Zheng, Y. Arsenic in tube well water in Bangladesh: health and economic impacts and implications for arsenic mitigation. *Bull. World Health Organ.* **90**, 839–846 (2012).
4. Shen, S., Li, X.-F., Cullen, W. R., Weinfeld, M. & Le, X. C. Arsenic Binding to Proteins. *Chem. Rev.* **113**, 7769–7792 (2013).
5. Hughes, M. F., Beck, B. D., Chen, Y., Lewis, A. S. & Thomas, D. J. Arsenic Exposure and Toxicology: A Historical Perspective. *Toxicol. Sci.* **123**, 305–332 (2011).
6. Mohan, D. & Pittman, C. U. Jr Arsenic removal from water/wastewater using adsorbents-A critical review. *J. Hazard. Mater.* **142**, 1–53 (2007).
7. Manning, B. A. & Goldberg, S. Adsorption and Stability of Arsenic(III) at the Clay Mineral−Water Interface. *Environ. Sci. Technol.* **31**, 2005–2011 (1997).
8. Manning, B. A., Fendorf, S. E. & Goldberg, S. Surface structures and stability of arsenic(III) on goethite: Spectroscopic evidence for inner-sphere complexes. *Environ. Sci. Technol.* **32**, 2383–2388 (1998).
9. Feng, X. *et al*. A Quantitative Model for the Coupled Kinetics of Arsenic. *Adsorption/DesorptiOxid. Manganese Oxides. Environ. Sci. Technol. Lett.* **5**, 175–180 (2018).
10. Manning, B. A., Fendorf, S. E., Bostick, B. & Suarez, D. L. Arsenic(III) Oxidation and Arsenic(V) Adsorption Reactions on Synthetic Birnessite. *Environ. Sci. Technol.* **36**, 976–981 (2002).
11. Luo, T., Cui, J., Hu, S., Huang, Y. & Jing, C. Arsenic Removal and Recovery from Copper Smelting Wastewater Using TiO_2. *Environ. Sci. Technol.* **44**, 9094–9098 (2010).
12. Guo, Q. *et al*. Enhanced Removal of Arsenic from Water by Synthetic Nanocrystalline Iowaite. *Sci. Rep*. **7** (2017).
13. Tian, Z. *et al*. Opposite effects of dissolved oxygen on the removal of As(III) and As(V) by carbonate structural Fe(II). *Sci. Rep*. **7** (2017).
14. Wu, C. *et al*. The double influence mechanism of pH on arsenic removal by nano zero valent iron: electrostatic interactions and the corrosion of Fe^0. *Environ. Sci. Nano* **4**, 1544–1552 (2017).
15. Chen, B., Zhu, Z., Ma, J., Qiu, Y. & Chen, J. Surfactant assisted Ce–Fe mixed oxide decorated multiwalled carbon nanotubes and their arsenic adsorption performance. *J. Mater. Chem. A* **1**, 11355 (2013).
16. Georgiou, Y., Perman, J. A., Bourlinos, A. B. & Deligiannakis, Y. Highly Efficient Arsenite [As(III)] Adsorption by an [MIL-100(Fe)] Metal–Organic Framework: Structural and Mechanistic Insights. *J. Phys. Chem. C.* **122**, 4859–4869 (2018).
17. Tabish, T. A., Memon, F. A., Gomez, D. E., Horsell, D. W. & Zhang, S. A facile synthesis of porous graphene for efficient water and wastewater treatment. *Sci. Rep*. **8**, (2018).
18. Wu, Z., Li, W., Webley, P. A. & Zhao, D. General and controllable synthesis of novel mesoporous magnetic iron oxide@ carbon encapsulates for efficient arsenic removal. *Adv. Mater.* **24**, 485–491 (2012).
19. Georgiou, Y. *et al*. Surface decoration of amine-rich carbon nitride with iron nanoparticles for arsenite (AsIII) uptake: The evolution of the Fe-phases under ambient conditions. *J. Hazard. Mater.* **312**, 243–253 (2016).
20. Daikopoulos, C. *et al*. Arsenite remediation by an amine-rich graphitic carbon nitride synthesized by a novel low-temperature method. *Chem. Eng. J.* **256**, 347–355 (2014).
21. Yavuz, C. T. *et al*. Low-Field Magnetic Separation of Monodisperse Fe3O4 Nanocrystals. *Science* **314**, 964–967 (2006).
22. Petala, E. *et al*. Magnetic Carbon Nanocages: An Advanced Architecture with Surface- and Morphology-Enhanced Removal Capacity for Arsenites. *ACS Sustain. Chem. Eng.* **5**, 5782–5792 (2017).
23. Yang, J. *et al*. High-Content, Well-Dispersed γ-Fe_2O_3 Nanoparticles Encapsulated in Macroporous Silica with Superior Arsenic Removal Performance. *Adv. Funct. Mater.* **24**, 1354–1363 (2014).
24. Georgiou, Y. *et al*. Mesoporous spinel $CoFe_2O_4$ as an efficient adsorbent for arsenite removal from water: high efficiency *via* control of the particle assemblage configuration. *Environ. Sci. Nano* **6**, 1156–1167 (2019).
25. Goldberg, S. & Johnston, C. T. Mechanisms of arsenic adsorption on amorphous oxides evaluated using macroscopic measurements, vibrational spectroscopy, and surface complexation modeling. *J. Colloid Interface Sci.* **234**, 204–216 (2001).
26. Goldberg, S. Competitive Adsorption of Arsenate and Arsenite on Oxides and Clay Minerals Contribution. *Soil. Sci. Soc. Am. J.* **66**, 413–421 (2002).
27. Gupta, A., Yunus, M. & Sankararamakrishnan, N. Zerovalent iron encapsulated chitosan nanospheres–A novel adsorbent for the removal of total inorganic Arsenic from aqueous systems. *Chemosphere* **86**, 150–155 (2012).
28. Su, C. & Puls, R. W. Arsenate and Arsenite Removal by Zerovalent Iron: Kinetics, Redox Transformation, and Implications for *in Situ* Groundwater Remediation. *Environ. Sci. Technol.* **35**, 1487–1492 (2001).
29. Georgiou, Y. *et al*. Surface decoration of amine-rich carbon nitride with iron nanoparticles for arsenite (As III) uptake: The evolution of the Fe-phases under ambient conditions. *J. Hazard. Mater.* **312**, 243–253 (2016).
30. Ge, J. *et al*. Joule-heated graphene-wrapped sponge enables fast clean-up of viscous crude-oil spill. *Nat. Nanotechnol.* **12**, 434–440 (2017).
31. Huang, C. *et al*. Progress in Research into 2D Graphdiyne-Based Materials. *Chem. Rev.* **118**, 7744–7803 (2018).
32. Li, Y., Xu, L., Liu, H. & Li, Y. Graphdiyne and graphyne: from theoretical predictions to practical construction. *Chem. Soc. Rev.* **43**, 2572 (2014).
33. Li, J. *et al*. Graphdiyne Sponge for Direct Collection of Oils from Water. *ACS Appl. Mater. Interfaces* **11**, 2591–2598 (2019).
34. Li, G. *et al*. Architecture of graphdiyne nanoscale films. *Chem. Commun.* **46**, 3256 (2010).
35. Xue, Y. *et al*. Anchoring zero valence single atoms of nickel and iron on graphdiyne for hydrogen evolution. *Nat. Commun.* **9**, 1460 (2018).
36. Hui, L. *et al*. Highly Efficient and Selective Generation of Ammonia and Hydrogen on a Graphdiyne-Based Catalyst. *J. Am. Chem. Soc.* **141**, 10677–10683 (2019).
37. Li, Y., Liu, T., Liu, H., Tian, M.-Z. & Li, Y. Self-Assembly of Intramolecular Charge-Transfer Compounds into Functional Molecular Systems. *Acc. Chem. Res.* **47**, 1186–1198 (2014).

38. Kile, D. E. & Chiou, C. T. Zhou, Huaidong., Li, Hui. & Xu, Ouyong. Partition of Nonpolar Organic Pollutants from Water to Soil and Sediment Organic Matters. *Environ. Sci. Technol.* **29**, 1401–1406 (1995).
39. Escher, B. I. & Schwarzenbach, R. P. Partitioning of Substituted Phenols in Liposome−Water, Biomembrane−Water, and Octanol−Water Systems. *Environ. Sci. Technol.* **30**, 260–270 (1996).
40. Noubigh, A., Mgaidi, A. & Abderrabba, M. Temperature Effect on the Distribution of Some Phenolic Compounds: An Experimental Measurement of 1-Octanol/Water Partition Coefficients. *J. Chem. Eng. Data* **55**, 488–491 (2010).
41. Anjaneyulu, Y., Marayya, R., Prabhakara Rao, R. & Kumar, P. V. S. Removal and recovery of priority pollutant phenols from industrial effluents using polyurethane foam medium. *Oil Chem. Pollut.* **7**, 349–365 (1990).
42. Prpich, G. P. & Daugulis, A. J. Polymer Development for Enhanced Delivery of Phenol in a Solid-Liquid Two-Phase Partitioning Bioreactor. *Biotechnol. Prog.* **20**, 1725–1732 (2004).
43. Li, Y. *et al*. Surface modification of hollow magnetic Fe3O4@NH2-MIL-101(Fe) derived from metal-organic frameworks for enhanced selective removal of phosphates from aqueous solution. *Sci. Rep*. **6**, (2016).
44. Ke, F. *et al*. Fumarate-based metal-organic frameworks as a new platform for highly selective removal of fluoride from brick tea. *Sci. Rep*. **8**, (2018).
45. Peng, Y. *et al*. A versatile MOF-based trap for heavy metal ion capture and dispersion. *Nat. Commun*. **9**, (2018).
46. Liang, L. *et al*. Carbon dioxide capture and conversion by an acid-base resistant metal-organic framework. *Nat. Commun*. **8**, (2017).
47. Zheng, T. *et al*. Overcoming the crystallization and designability issues in the ultrastable zirconium phosphonate framework system. *Nat. Commun.* **8**, 15369 (2017).
48. Yang, J.-C. & Yin, X.-B. CoFe2O4@MIL-100(Fe) hybrid magnetic nanoparticles exhibit fast and selective adsorption of arsenic with high adsorption capacity. *Sci. Rep.* **7**, 40955 (2017).
49. Wang, C., Liu, X., Chen, J. P. & Li, K. Superior removal of arsenic from water with zirconium metal-organic framework UiO-66. *Sci. Rep*. **5**, (2015).
50. Kumar, P. *et al*. Metal-organic frameworks: Challenges and opportunities for ion-exchange/sorption applications. *Prog. Mater. Sci.* **86**, 25–74 (2017).
51. Jian, M. *et al*. Self-assembled one-dimensional MnO_2@zeolitic imidazolate framework-8 nanostructures for highly efficient arsenite removal. *Environ. Sci. Nano* **3**, 1186–1194 (2016).
52. Usman, M., Katsoyiannis, I., Mitrakas, M., Zouboulis, A. & Ernst, M. Performance Evaluation of Small Sized Powdered Ferric Hydroxide as Arsenic Adsorbent. *Water* **10**, 957 (2018).
53. Luo, J. *et al*. Arsenic adsorption on α-MnO2 nanofibers and the significance of (1 0 0) facet as compared with (1 1 0). *Chem. Eng. J.* **331**, 492–500 (2018).
54. De, D., Aniya, V. & Satyavathi, B. Application of an agro-industrial waste for the removal of As (III) in a counter-current multiphase fluidized bed. *Int. J. Environ. Sci. Technol.* **16**, 279–294 (2019).
55. Wang, W. *et al*. Effect of humic acid on ciprofloxacin removal by magnetic multifunctional resins. *Sci. Rep*. **6**, (2016).
56. Chiou, C. T., Peters, L. J. & Freed, V. H. A Physical Concept of Soil-Water Equilibria for Nonionic Organic Compounds. *Science* **206**, 831–832 (1979).
57. Chen, B., Zhou, D. & Zhu, L. Transitional Adsorption and Partition of Nonpolar and Polar Aromatic Contaminants by Biochars of Pine Needles with Different Pyrolytic Temperatures. *Environ. Sci. Technol.* **42**, 5137–5143 (2008).
58. Gulrajani, M. L. Degumming of silk. *Rev. Prog. Color. Relat. Top.* **22**, 79–89 (2008).
59. Choudhury, M., Devi, D. & Laboratory, S. Impact of high temperature and pressure on sericin scouring of muga silk cocoons. *Indian J Fibre Text Res* 4 (2016).
60. Huo, L., Zeng, X., Su, S., Bai, L. & Wang, Y. Enhanced removal of As (V) from aqueous solution using modified hydrous ferric oxide nanoparticles. *Sci. Rep.* **7**, 40765 (2017).
61. Linstrom, P. NIST Chemistry WebBook, NIST Standard Reference Database 69. https://doi.org/10.18434/t4d303 (1997).
62. Sudhakar, C. *et al*. Species-Specific Uptake of Arsenic on Confined Metastable 2-Line Ferrihydrite: A Combined Raman-X-Ray Photoelectron Spectroscopy Investigation of the Adsorption Mechanism. *ACS Sustain. Chem. Eng.* **6**, 9990–10000 (2018).
63. Canaval, L. R., Lutz, O. M. D., Weiss, A. K. H., Huck, C. W. & Hofer, T. S. A Dissociative Quantum Mechanical/Molecular Mechanical Molecular Dynamics Simulation and Infrared Experiments Reveal Characteristics of the Strongly Hydrolytic Arsenic(III). *Inorg. Chem.* **53**, 11861–11870 (2014).
64. Han, M. *et al*. Bio-butanol sorption performance on novel porous-carbon adsorbents from corncob prepared via hydrothermal carbonization and post-pyrolysis method. *Sci. Rep.* **7**, 11753 (2017).
65. Masel, R. I. *Principles of adsorption and reaction on solid surfaces*. (Wiley (1996).
66. Mirsal, I. Soil Pollution. (Springer Berlin Heidelberg. https://doi.org/10.1007/978-3-540-70777-6 (2008).
67. Mouzourakis, E., Georgiou, Y., Louloudi, M., Konstantinou, I. & Deligiannakis, Y. Recycled-tire pyrolytic carbon made functional: A high-arsenite [As(III)] uptake material PyrC350®. *J. Hazard. Mater.* **326**, 177–186 (2017).
68. Berner, E. K. & Berner, R. A. *Global environment: water, air, and geochemical cycles*. (Prentice Hall (1996).
69. Jain, A. & Loeppert, R. H. Effect of Competing Anions on the Adsorption of Arsenate and Arsenite by Ferrihydrite. *J. Environ. Qual.* **29**, 1422–1430 (2000).
70. Georgiou, Y., Dimos, K., Beltsios, K., Karakassides, M. A. & Deligiannakis, Y. Hybrid [polysulfone–Zero Valent Iron] membranes: Synthesis, characterization and application for As III remediation. *Chem. Eng. J.* **281**, 651–660 (2015).
71. Rapti, S. *et al*. Rapid, green and inexpensive synthesis of high quality UiO-66 amino-functionalized materials with exceptional capability for removal of hexavalent chromium from industrial waste. *Inorg. Chem. Front.* **3**, 635–644 (2016).
72. Karageorgou, D. *et al*. Antibacterial and Algicidal Effects of Porous Carbon Cuboid Nanoparticles. *ACS Omega* **4**, 4991–5001 (2019).
73. Moularas, C., Georgiou, Y., Adamska, K. & Deligiannakis, Y. Thermoplasmonic Heat Generation Efficiency by Nonmonodisperse Core–Shell Ag^0@SiO_2 Nanoparticle Ensemble. *J. Phys. Chem. C.* **123**, 22499–22510 (2019).
74. Barra, C. M. & dos Santos, M. M. C. Speciation of Inorganic Arsenic in Natural Waters by Square-Wave Cathodic Stripping Voltammetry. *Electroanalysis* **13**, 1098–1104 (2001).
75. Pallier, V., Serpaud, B., Feuillade-Cathalifaud, G. & Bollinger, J.-C. Comparison of voltammetric and AAS methods for As(III) quantification in presence of iron species in model water samples with a low mineral content. *Int. J. Environ. Anal. Chem.* **91**, 1–16 (2011).
76. Ladeira, A. C. Q. & Ciminelli, V. S. T. Adsorption and desorption of arsenic on an oxisol and its constituents. *Water Res.* **38**, 2087–2094 (2004).
77. Liu, B., Jian, M., Liu, R., Yao, J. & Zhang, X. Highly efficient removal of arsenic(III) from aqueous solution by zeolitic imidazolate frameworks with different morphology. *Colloids Surf. Physicochem. Eng. Asp.* **481**, 358–366 (2015).
78. Huo, J.-B. *et al*. Magnetic responsive Fe 3 O 4 -ZIF-8 core-shell composites for efficient removal of As(III) from water. *Colloids Surf. Physicochem. Eng. Asp.* **539**, 59–68 (2018).
79. Audu, C. O. *et al*. The dual capture of As^V and As^{III} by UiO-66 and analogues. *Chem. Sci.* **7**, 6492–6498 (2016).
80. Folens, K. *et al*. Fe_3O_4@MIL-101 - A Selective and Regenerable Adsorbent for the Removal of As Species from Water: Fe_3O_4@MIL-101 - A Selective and Regenerable Adsorbent for the Removal of As Species from Water. *Eur. J. Inorg. Chem.* **2016**, 4395–4401 (2016).

Acknowledgements
Authors we would like to thank "Tsiakiris Georgios Silk Company", Alexandroupoli, Greece, for providing Silk Fabric (SF). The research work of M. J. Manos, was supported by the Hellenic Foundation for Research and Innovation (H.F.R.I.) under the "First Call for H.F.R.I. Research Projects to support Faculty members and Researchers and the procurement of high-cost research equipment grant" (Project Number: 348).

Author contributions
Y.G has conducted the experiential and theoretical work on As-uptake, and part of materials characterization. S.R. has conducted the synthesis of ZrMOF and part of materials characterization. A.M. has conducted the synthesis of silk-grated ZrMOF@SF_d,G.A. has conducted the SEM analysis, M.M. was responsible for the design and characterisation of the ZrMOF as well as part of manuscript writing, M.L. was responsible for the design and characterisation of the ZrMOF@SF_d as well as part manuscript writing. Y.D. was responsible for the design of the project, the theoretical analysis of data, analysis of the structural data and manuscript writing. All authors have approved the final version.

Competing interests
The authors declare no competing interests.

Additional information
Supplementary information is available for this paper at https://doi.org/10.1038/s41598-020-66091-w.

Correspondence and requests for materials should be addressed to Y.D.

Reprints and permissions information is available at www.nature.com/reprints.

Publisher's note Springer Nature remains neutral with regard to jurisdictional claims in published maps and institutional affiliations.